PHYSICAL REVIEW A **80**, 050302(R) (2009)

Robust control of individual nuclear spins in diamond

Benjamin Smeltzer, Jean McIntyre, and Lilian Childress
Department of Physics and Astronomy, Bates College, Lewiston, Maine 04240, USA
(Received 25 September 2009; published 25 November 2009)

Isolated nuclear spins provide a promising building block for quantum information science, motivating development of techniques to characterize, control, and detect them in suitable systems. Working with the nitrogen-vacancy center in diamond, we demonstrate robust initialization, manipulation, and readout of individual ^{13}C, ^{15}N, and ^{14}N nuclear spins and identify a mechanism to extend our results to arbitrary magnetic field environments. These techniques enable precise characterization of nuclear-spin hyperfine parameters and coherence properties and may pave the way for nuclear-spin-based quantum information architectures in diamond.

DOI: 10.1103/PhysRevA.80.050302 PACS number(s): 03.67.Lx, 76.70.Hb, 76.90.+d, 33.25.+k

The long coherence times of nuclear spins have attracted considerable interest for applications in quantum information science [1–8], offering the potential for devices exhibiting coherent evolution over time scales exceeding several seconds [9]. Nevertheless, scalable control and detection of single nuclear spins remains an outstanding challenge. Some of the most promising approaches use electronic spins as an intermediary to access nuclear spins in solid state [2–6,10,11] or atomic [7,8] systems. While atomic systems enable optical preparation and near-perfect isolation of nuclear spins, nanoscale solid-state systems offer the possibility of manipulating and coupling spins on fast time scales. Atomlike defects in solids [12–20] offer an intriguing interpolation between these approaches, allowing optical techniques in a setting amenable to fast control.

We use the electronic spin of the negatively charged nitrogen-vacancy (NV), an atomlike defect, to access individual nuclear spins in the diamond lattice. Even at room temperature, the NV spin is readily polarized and manipulated with optical and microwave fields [21], yet it can exhibit millisecond coherence times [15,16]. Moreover, its hyperfine interactions with nearby nuclear spins have allowed observation of nuclear-spin precession, entanglement, and electron-nuclear-spin quantum gates [13,14,16,17]. With electronic or optical transitions for long-range interactions and long-lived proximal nuclear spins for quantum memory, the NV center has become a strong candidate for quantum computation [12,17,20] and communication [18] applications.

Three nuclear-spin species commonly interact with the NV center, offering different properties that lend themselves to different applications. Experimental manipulation of nuclear spins associated with the NV center has emphasized $I=\frac{1}{2}$ ^{13}C nuclear spins, focusing on the nearest-neighbor lattice sites [13,14,16,17,19]. With a large hyperfine coupling, nearest-neighbor ^{13}C nuclear spins provide faster interactions but shorter coherence times [16,17]; like all ^{13}C nuclei, they occur randomly as isotopic impurities in the lattice. In contrast, the ^{14}N and ^{15}N species are weakly coupled [22], but they occur deterministically on the nitrogen of the NV center in natural (^{14}N) and isotope implanted (^{15}N) diamond [23,24]. Scalable schemes—based, for example, on arrays of dipole-coupled electron-nuclear-spin pairs or optically connected quantum registers [17,18,20]—are thus likely to favor the consistent properties of the nitrogen nuclear spins. Furthermore, the longest electron-spin coherence times have been observed only in highly isotopically purified, unimplanted diamond [15,16], in which ^{13}C and ^{15}N spins are exceedingly rare. These considerations point toward the development of control techniques for ^{15}N and ^{14}N as well as ^{13}C nuclear spins.

In this Rapid Communication, we demonstrate dynamic polarization, resonant manipulation, and optical detection of single ^{13}C, ^{14}N, and ^{15}N nuclear spins associated with the NV center in diamond. These techniques do not rely on $I=\frac{1}{2}$ spin properties or weak (selective) electron-spin resonance (ESR), and give rise to signals as strong as the NV ESR signal. Moreover, the techniques are related, sharing a common origin in the nonsecular components of the hyperfine interaction: Electron-nuclear-spin flip-flops allow robust polarization [24], greatly enhance the Rabi frequency for nuclear magnetic resonance (NMR) [19], and enable direct optical readout of the nuclear spin. These mechanisms are robust to small magnetic field shifts up to a few gauss, and we show that it may be possible to extend them to work in arbitrary magnetic fields.

In our experiments, NV centers in chemical vapor deposition (CVD) –grown high-purity diamond (Sumitomo, natural isotopic abundance) are isolated using confocal microscopy, allowing selection of NV centers with different proximal nuclear spins. The centers are illuminated by 4 mW of 532 nm light for polarization and fluorescence detection, while Helmholtz coils and/or a permanent magnet apply magnetic fields between 0 and 500 G. Electron-spin transitions are driven by microwaves (MW) via a 25 μm copper wire mounted on the sample; the same wire carries radio-frequency (rf) signals resonant with nuclear-spin transitions.

The NV center in diamond has an electronic spin $S=1$ in both its ground state (g.s.) and optically excited state (e.s.) [21], and both orbital configurations exhibit a zero-field splitting between the $m_s=0$ and $m_s=\pm 1$ spin projections along the NV axis $\hat{z}$ [$\Delta=2.87$ GHz (g.s.) or $D=1.42$ GHz (e.s.)] [23]. The electronic structure of the NV center also includes at least one long-lived spin singlet state of intermediate energy that preferentially depopulates the e.s. $m_s=\pm 1$ states and decays into the g.s. $m_s=0$ state [21]. Under optical illu-

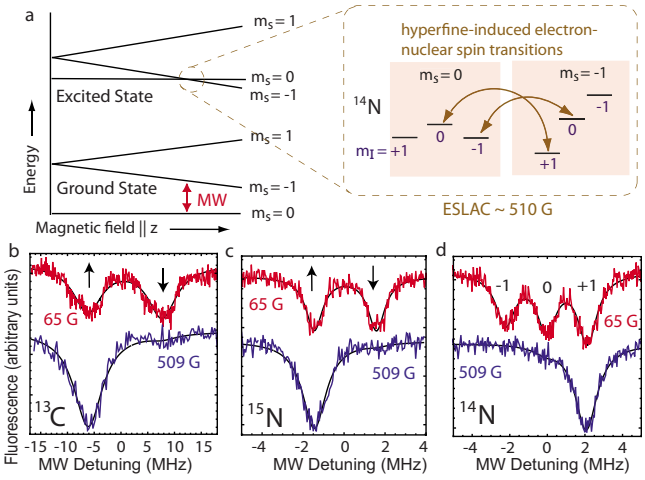

FIG. 1. (Color online) (a) Electronic-spin states of the NV center, showing the ESLAC near 510 G. Inset shows hyperfine levels and transitions for the ^{14}N isotope. (b)–(d) ESR for an NV center coupled to a proximal nuclear spin in $B=65$ G (top) and 509 G (bottom). (b) A third-shell ^{13}C [22,25] exhibits $P=91(5)\%$ polarization at 509 G; parentheses indicate one standard deviation statistical error in the final digit. (c) ^{15}N: $P=95(3)\%$. (d) ^{14}N: $P=95(3)\%$.

mination, $m_s=\pm 1$ states can thus cross over to the dark singlet state, reducing their initial fluorescence relative to $m_s=0$; after a few 100 ns, the metastable state decays, polarizing the electronic spin into $m_s=0$. The singlet state thereby provides the mechanism for optical polarization and detection of the electronic spin state [21].

In certain magnetic fields, optical spin polarization can be extended to proximal nuclei [23,24]. Near 510 G$\|\hat{z}$, the e.s. $m_s=-1$ and $m_s=0$ states become degenerate [see Fig. 1(a)], allowing electron-nuclear-spin flip-flops to occur near resonantly; repeated cycling through the singlet state thus results in polarization into $m_s=0$ with maximal m_I [see Figs. 1(b)–1(d)]. This mechanism was previously used to polarize ^{15}N and nearest-neighbor ^{13}C nuclear spins [24]; we observe that it polarizes the $I=1$ species ^{14}N via the two-step process illustrated in Fig. 1(a). While non-nearest-neighbor ^{13}C nuclei may also be polarized in this manner [see Fig. 1(b)], not all ^{13}C locations exhibit such polarization (data not shown) most likely because their hyperfine axes are not aligned in the ground and excited states [22,25].

Optical pumping at the excited-state level-anticrossing (ESLAC) provides the polarization necessary for NMR measurements. Working within the $m_s=-1$ manifold, we measure the nuclear-spin projection along $\hat{z}$ as a function of rf frequency and duration (see Fig. 2) and fit our data to the expected form for square pulse excitation to extract the resonance frequencies ω_n and Rabi frequencies Ω_n for all three nuclear-spin species. Observed values of ω_n are consistent with published values [22], but the Rabi frequencies Ω_n greatly exceed the naive expectation $\Omega_n=|\gamma_n B_{\mathrm{rf}}|\sim$ a few kHz (we measure $B_{\mathrm{rf}}\sim 5-10$ G). Indeed, the nuclear-spin nutation rates are dominated by a second order process involving an electron-spin flip followed by an electron-nuclear-spin flip-flop, with $\Omega_n\approx\gamma_n B_{\mathrm{rf}}+A_\perp g\mu_B B_{\mathrm{rf}}/\Delta$ [19]. The enhanced

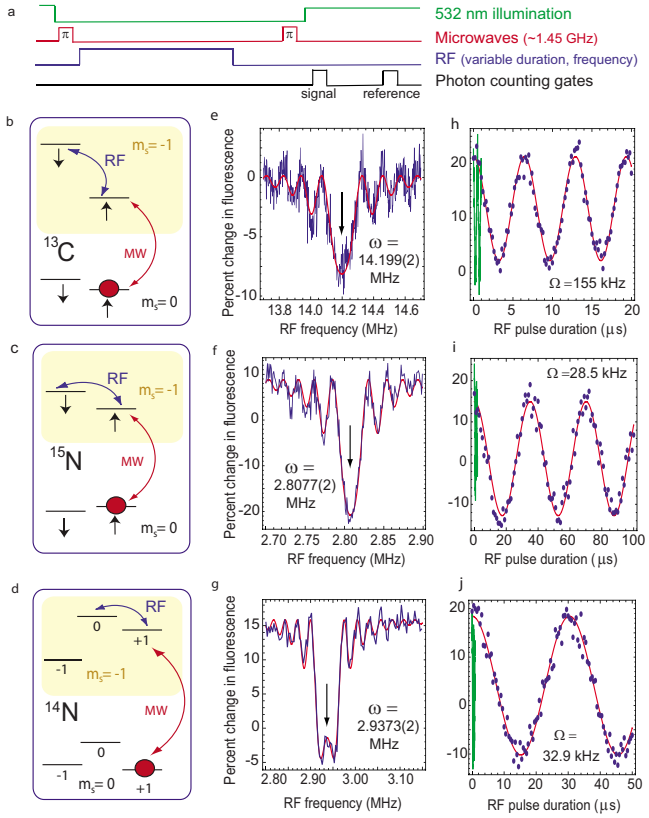

FIG. 2. (Color online) (a) Pulse sequence. Following polarization, a MW π pulse drives the system into the g.s. $m_s=-1$ state, where rf excites nuclear-spin transitions. A second MW π pulse flips the electron spin back into $m_s=0$, and subsequent fluorescence detection reveals the average nuclear-spin projection. All data are taken in a magnetic field of 509 G$\|\hat{z}$. Data for ^{13}C, ^{15}N, and ^{14}N are shown in (b,e,h), (c,f,i), and (d,g,j), respectively. (b)–(d) g.s. energy level diagrams for hyperfine levels; arrows indicate transitions driven by rf and MW; shading indicates the $m_s=-1$ manifold. (e)–(g) Fluorescence change [(signal-reference)/reference] vs rf frequency. Fitted resonance frequencies are given with one standard deviation statistical error. (h)–(j) Fluorescence vs rf pulse duration on resonance with a sinusoidal fit. Short-time data show contrast of electron-spin nutations for comparison.

Rabi frequency occurs for all nuclear-spin species, enabling fast manipulation with low demands on rf power.

The contrast of nuclear-spin nutations shown in Fig. 2 is as great or greater than the ESR signal because the polarization and readout mechanisms are robust to electron-spin dephasing caused by the fluctuating nuclear-spin bath. Earlier nuclear-spin polarization and readout schemes that relied on nuclear-spin-selective MW pulse(s) to map nuclear-spin populations onto polarizable and measureable electron-spin populations [13,16,17] have worked poorly for ^{15}N and ^{14}N because the nitrogen g.s. hyperfine splittings do not greatly exceed the electron-spin dephasing rate. In contrast, the large e.s. hyperfine parameters (A$\sim$50 MHz [23,25,26]) permit the polarization mechanism described above to function over a range of several gauss [24], reducing sensitivity to the fluctuating spin bath environment. Moreover, the strong e.s. hyperfine interaction also allows robust readout of the nuclear-spin state: while the $m_s=0$ state with maximal nuclear-spin

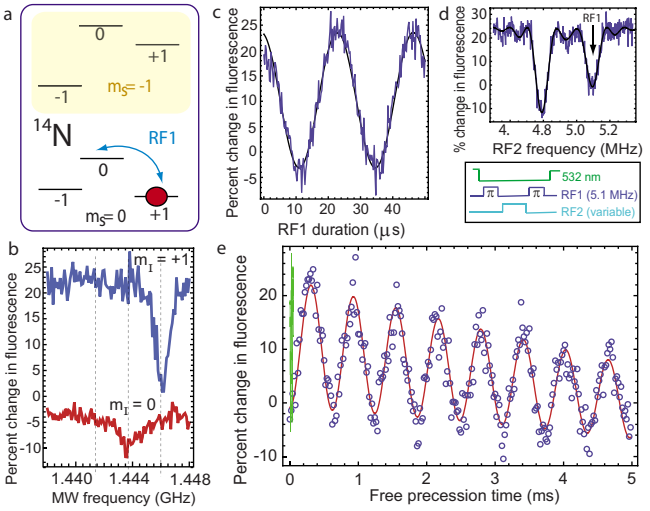

FIG. 3. (Color online) (a) Energy levels for g.s. $m_s=0$ ^{14}N nuclear-spin manipulation. (b) Pulsed ESR spectra starting in $m_s=0$, $m_I=1$ (top) or $m_s=0$, $m_I=0$ (bottom). Dashed lines indicate expected ESR positions for the three hyperfine levels. (c) Nuclear Rabi nutations within the $m_s=0$ manifold. (d) NMR spectrum obtained using the pulse sequence illustrated. A fit to the expected square-pulse line shape yields resonant frequencies $\omega_1/(2\pi)=5.094(1)$ MHz and $\omega_2/(2\pi)=4.7908(7)$ MHz, while the lower frequency line is deeper owing to the two-step polarization process for $m_I=-1$. (e) Nuclear Ramsey fringe experiment. The downward trend is likely due to electron-spin relaxation, which occurs at a rate $T_1\approx$ few ms at room temperature [14,21].

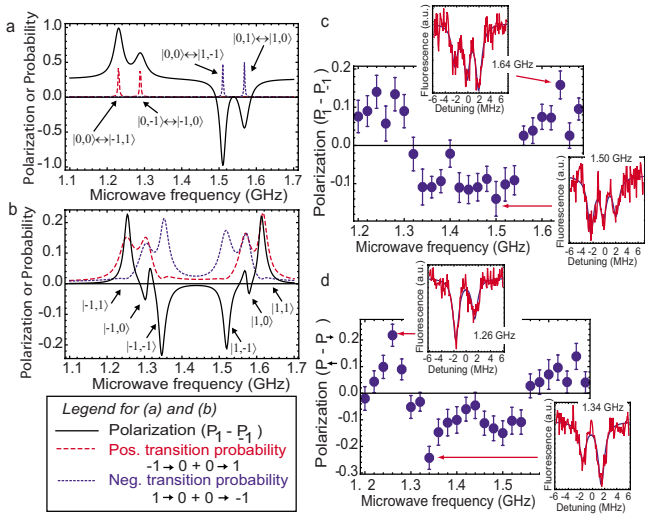

FIG. 4. (Color online) (a) Theoretical transition probabilities and equilibrium polarization for ^{14}N with $\mathbf{B}_0=50\hat{z}$ G, $g\mu_B\mathbf{B}_1=20\hat{z}$ MHz, A=50 MHz, $P=-5$ MHz, D=1.42 GHz, $\gamma_n=0.3077$ kHz/G, $\gamma_e=2.8$ MHz/G, $\gamma=2.5\Gamma$, and $k_{eq}=10^{-5}\Gamma$. Resonances are indicated using the notation $|m_s,m_I\rangle$. (b) Same as for (a), but with $g\mu_B\mathbf{B}_1=20\hat{x}+20\hat{z}$ MHz and $\mathbf{B}_0=40\hat{x}+48\hat{z}$ G. The initial state in each resonance is $m_s=0$, $m_I=0$, -1, or $+1$; the final state in each resonance is noted as $|m_s,m_I\rangle$. (c) Polarization of ^{14}N in $\mathbf{B}_0=40\hat{x}+48\hat{z}$ G. Error bars indicate one standard deviation (statistical). Insets show ESR signal and fit for specific data points. (d) Polarization of ^{15}N under the same experimental conditions.

projection fluoresces strongly, electron-nuclear-spin flip-flops in the excited state cause the other nuclear-spin projections to pass through the dark singlet state one or more times during the polarization process, leading to reduced fluorescence. To illustrate the readout process, Fig. 3(b) compares an ESR spectrum with $m_I=+1$ (^{14}N) to one with $m_I=0$ [created using an NMR π pulse on the transition indicated in Fig. 3(a)]. The ESR spectra corroborate the nuclear-spin projection and illustrate a significantly reduced fluorescence level for $m_I=0$ as compared to $m_I=1$. While our measurements of this effect are aimed at direct nuclear-spin readout, since our experiments have concluded the same mechanism has been explored for applications in enhanced electron-spin measurement [26].

The preparation, control, and detection techniques described above enable straightforward measurement of nuclear-spin energy levels and coherence properties. As an example, ^{14}N hyperfine parameters are calculated from NMR resonance frequencies for ^{14}N within the $m_s=0$ [Fig. 3(d)] and $m_s=1$ manifolds [see Fig. 2(g); we observe the other resonance at 6.9580(2) MHz, data not shown]. We thus determine $A_\parallel=-2.162(2)$ MHz and $P=-4.945(5)$ MHz for this NV center, demonstrating an improved precision over published values [22]. Coherence properties of individual nuclear spins are also readily obtained: Fig. 3(e) shows a 2 kHz detuned Ramsey fringe experiment on the transition indicated in Fig. 3(a). Although coherence properties for specific NV centers will vary with the mesoscopic distribution of ^{13}C impurities, the long dephasing time $T_2^*\sim$ few ms observed here bodes well for ^{14}N-based schemes. In short, these techniques open the door for complete characterization of individual nuclear spins associated with the NV center.

Resonant rf excitation can drive transitions in arbitrary nuclear-spin species in any magnetic field, but the polarization and direct readout mechanisms function only in the vicinity of the ESLAC near 510 G. This limitation is severe, especially for applications requiring optical interconnections between NV centers [18,20] or stimulated emission-depletion techniques for subwavelength resolution [27]. Near the ESLAC, any light used to excite electronic transitions can destroy information stored in nuclear spins. While magnetic field switching techniques developed in the context of fast field cycling NMR [28] may allow rapid transitions between two magnetic field regimes, it may also be possible to induce optical nuclear-spin polarization and readout in arbitrary magnetic fields though judicious application of microwaves.

In any magnetic field, the electron-nuclear-spin transitions that lead to nuclear-spin polarization and readout can be brought into resonance by MW excitation within the e.s. manifold. However, typically the microwaves will only flip the electron spin, circumventing hyperfine-induced flip-flops. To drive the desired transitions, higher-order processes must prevail: for example, the axial ($\|\hat{z}$) component of the microwave magnetic field and the nonsecular hyperfine terms can induce electron-nuclear-spin flip-flops through a second-order process, while transverse components ($\perp\hat{z}$) of the static and microwave fields yield similar results through a third-order process.

We model microwave-induced polarization using the e.s. Hamiltonian for the (N-V)-^{14}N spin system

$$H = DS_z^2 + PI_z^2 + (\mathbf{B}_0 + \mathbf{B}_1 \cos \omega t) \cdot (g\mu_B \mathbf{S} - \gamma_n \mathbf{I}) + A\mathbf{I} \cdot \mathbf{S},$$

with a quadrupole splitting P, an isotropic g-factor, and a contact hyperfine interaction A [25]. We then use Floquet theory [29] to calculate the probability for each nuclear-spin-changing transition in the excited state as a function of the microwave frequency ω. In the case of ^{14}N, these probabilities can be incorporated into a three-level rate equation model because its nuclear-spin quantization axis is unaffected by electronic transitions in moderate magnetic fields. Multiplying the transition probabilities by an excitation rate γ (for transitions within the $m_s=0$ manifold) or Γ (for transitions between the $m_s=0$ and $m_s=\pm 1$ manifolds) yields the transition rates; we incorporate a depolarization rate k_{eq} to complete the model, from which we predict the equilibrium nuclear-spin polarization $P_{+1}-P_{-1}$ [24]. The details of this model will be published elsewhere. Figure 4(a) shows calculated ^{14}N nuclear-spin-flip probabilities and equilibrium polarization for static and oscillatory magnetic fields $\mathbf{B}_0$ and $\mathbf{B}_1$ oriented along $\hat{z}$, while Fig. 4(b) illustrates the same quantities for off-axis magnetic fields.

Experimental verification of the model is limited by the geometry of our sample mount to measurements with $\mathbf{B}_1 \sim 45°$ from the NV axis. Working in a static magnetic field $\mathbf{B}_0 = 40\hat{x} + 48\hat{z}$, we apply optical excitation and microwaves of varying frequency before taking a g.s. ESR spectrum. We fit the g.s. ESR signals with three (or two, for ^{15}N) equal-width Lorentzians and use the depth of the fits to estimate the population in each of the nuclear-spin projections. We thereby observe a small degree of polarization for both ^{14}N and ^{15}N nuclear spins [see Figs. 4(c) and 4(d)], and our results in Fig. 4(c) agree qualitatively with the model predictions in Fig. 4(b).

Although our experiments are currently constrained by the orientation of $\mathbf{B}_1$, our model indicates that precise orientation of $\mathbf{B}_0$ and $\mathbf{B}_1$ [30] may allow full polarization of ^{14}N [Fig. 4(a)]. Moreover, because each polarization step involves the metastable singlet state, such a polarization technique will also provide a direct nuclear-spin readout mechanism. With careful engineering, it may be possible to enjoy the robust nuclear-spin polarization and readout now available at the ESLAC at arbitrary magnetic fields.

In conclusion, we have demonstrated initialization, manipulation, and direct readout of nuclear spins associated with the NV center in diamond and proposed a mechanism to extend these techniques to other magnetic field regimes. Such control over nuclear spins has ramifications for a broad range of applications in quantum information science. Moreover, these techniques enable measurements of nuclear-spin parameters, interactions, and coherence properties that may guide development of future nuclear-spin-based devices.

Note added. Recently, similar work was reported [26].

The authors acknowledge Yuanyuan Jiang and Gabriel Ycas for their work building and characterizing the experimental apparatus and writing software to run it. We thank Mikhail Lukin, Jonathan Hodges, and Gurudev Dutt for valuable conversations. This work was supported by funds from Research Corporation and from Bates College. J.M. and B.S. acknowledge support from HHMI.

[1] L. Vandersypen and I. Chuang, Rev. Mod. Phys. **76**, 1037 (2004).
[2] B. Kane, Nature (London) **393**, 133 (1998).
[3] J. Baugh *et al.*, Phys. Rev. A **73**, 022305 (2006).
[4] W. M. Witzel and S. Das Sarma, Phys. Rev. B **76**, 045218 (2007).
[5] J. J. L. Morton *et al.*, Nature (London) **455**, 1085 (2008).
[6] P. Cappellaro, L. Jiang, J. S. Hodges, and M. D. Lukin, Phys. Rev. Lett. **102**, 210502 (2009).
[7] A. Gorshkov *et al.*, Phys. Rev. Lett. **102**, 110503 (2009).
[8] M. Feng, Y. Y. Xu, F. Zhou, and D. Suter, Phys. Rev. A **79**, 052331 (2009).
[9] T. D. Ladd, D. Maryenko, Y. Yamamoto, E. Abe, and K. M. Itoh, Phys. Rev. B **71**, 014401 (2005).
[10] J. R. Petta *et al.*, Phys. Rev. Lett. **100**, 067601 (2008).
[11] A. Bracker *et al.*, Phys. Rev. Lett. **94**, 047402 (2005).
[12] J. Wrachtrup and F. Jelezko, J. Phys.: Condens. Matter **18**, S807 (2006).
[13] F. Jelezko *et al.*, Phys. Rev. Lett. **93**, 130501 (2004).
[14] P. Neumann *et al.*, Science **320**, 1326 (2008).
[15] G. Balasubramanian *et al.*, Nature Mater. **8**, 383 (2009).
[16] N. Mizuochi *et al.*, Phys. Rev. B **80**, 041201(R) (2009).
[17] M. V. G. Dutt *et al.*, Science **316**, 1312 (2007).
[18] L. Childress, J. M. Taylor, A. S. Sorensen, and M. D. Lukin, Phys. Rev. Lett. **96**, 070504 (2006).
[19] L. Childress *et al.*, Science **314**, 281 (2006).
[20] L. Jiang, J. M. Taylor, A. S. Sorensen, and M. D. Lukin, Phys. Rev. A **76**, 062323 (2007).
[21] N. B. Manson, J. P. Harrison, and M. J. Sellars, Phys. Rev. B **74**, 104303 (2006).
[22] S. Felton *et al.*, Phys. Rev. B **79**, 075203 (2009).
[23] G. D. Fuchs *et al.*, Phys. Rev. Lett. **101**, 117601 (2008).
[24] V. Jacques *et al.*, Phys. Rev. Lett. **102**, 057403 (2009).
[25] A. Gali, e-print arXiv:0905.1169.
[26] M. Steiner *et al.*, e-print arXiv:0909.2783.
[27] E. Rittweger *et al.*, Nat. Photonics **3**, 144 (2009).
[28] E. Anoardo, G. Galli, and G. Ferrante, Appl. Magn. Reson. **20**, 365 (2001).
[29] J. Shirley, Phys. Rev. **138**, B979 (1965).
[30] T. P. M. Alegre, A. C. Torrezan, and G. Medeiros-Ribeiro, Appl. Phys. Lett. **91**, 204103 (2007).